Nanoscale

PAPER

View Article Online
View Journal | View Issue

Cite this: *Nanoscale*, 2023, **15**, 12728

InSb-based saturable absorbers for ultrafast photonic applications

Lihui Pang, *[a,d] Rongfeng Wang,[a,d] Qiyi Zhao,[b] Meng Zhao,[a,d] Le Jiang,[a,d] Xiaogang Zhang,[a] Rongqian Wu,[a,d] Yi Lv [a,d] and Wenjun Liu *[c]

Received 27th March 2023,
Accepted 4th July 2023

DOI: 10.1039/d3nr01416a

rsc.li/nanoscale

Sb-related III–V compounds have recently gained great research interest owing to their excellent optical and electrical characteristics, which provide many possibilities in photonics and electronics. This study investigated the application of InSb films in ultrafast photonics. An InSb film was fabricated on the tapered zone of a microfiber, and its saturation intensity, modulation depth, and non-saturable loss were determined as 119.8 MW cm^{-2}, 23.5%, and 27.3%, respectively. The structure of the electronic band and density of states of InSb were theoretically calculated. Notably, mode-locked and Q-switched fiber lasers were realised by incorporating the InSb-microfiber device into two different Er-doped fiber cavities. In the Q-switching state, the narrowest pulse duration was measured as 1.756 μs with a maximum single-pulse energy of 221.95 nJ and a signal-to-noise ratio of 60 dB. In the mode-locking operation, ultrafast lasers with a high signal-to-noise ratio (70 dB), a pulse width as narrow as 265 fs and a repetition rate of 49.51 MHz were acquired. Besides, the second-harmonic mode-locked state was built with an output power of 13.22 mW. In comparison with the reported laser performance with 2D materials as saturable absorbers, the InSb-based mode-locked and Q-switched fiber lasers proposed herein exhibit better comprehensive performance.

Introduction

Pulsed lasers have been proved to be indispensable in a broad scope of applications, including biomedicine, optical sensing, spectroscopy, and ultra-precision machining.[1,2] At present, there are two technologies for generating laser pulses: Q-switched and mode-locked methods. An effective way to trigger these pulsed operations is to use nonlinear optical materials with saturable absorption properties, which can switch between different absorption conditions on short timescales and generate pulsed lasers.[3–5] In the past decade, the enormous progress of 2D materials has motivated their application in pulsed lasers and in the field of ultrafast optics.[6–9] Most 2D materials inherently exhibit stronger nonlinear optical responses and light–matter interactions compared to their bulk counterparts, making them widely used in portable photonic applications.[10] Based on their outstanding attributes such as wide spectral bands, good mechanical flexibility, high damage thresholds, and fine compatibility with optical components, 2D materials have been widely used in nonlinear optical devices, such as photonic chips, all-optical modulators, optical sensors, saturable absorbers (SAs), and four-wave mixing generators.[11–14] In particular, SA devices based on 2D materials for pulsed fiber lasers have been extensively investigated.[15–18] To date, 2D SA materials include transition metal dichalcogenides, MXenes, single-element 2D materials, topological insulators, perovskites, and other divergent 2D materials.[19–24] Remarkable development has been achieved in pulsed lasers with 2D SAs. Using graphene as the SA, 10 GHz laser pulse outputs have been achieved in an ultrafast fiber laser.[25] A short pulse duration of 67 fs was observed in a WS2 ultrafast fiber laser.[26] Pulsed fiber lasers with good stability based on 2D SAs have also been developed.[27,28] In addition, the saturable absorption features of 2D materials have been demonstrated in the long-wavelength band.[29] Despite the exciting success these 2D SA materials have achieved, research in this regard is insufficient. Thus, exploration of 2D materials with stable chemical characteristics, high optical nonlinearity, fast dynamics, and good absorption efficiency is required.

Over the past decade, owing to their remarkable physical and chemical characteristics, low-dimensional III–V com-

[a]*Shaanxi Provincial Center for Regenerative Medicine and Surgical Engineering, First Affiliated Hospital, Xi'an Jiaotong University, Xi'an 710061, China. E-mail: lhpang@mail.xjtu.edu.cn*
[b]*School of Science, Xi'an University of Posts and Telecommunications, Xi'an 710121, China*
[c]*State Key Laboratory of Information Photonics and Optical Communications, School of Science, Beijing University of Posts and Telecommunications, Beijing 100876, China. E-mail: jungliu@bupt.edu.cn*
[d]*National Local Joint Engineering Research Center of Precise Surgery & Regenerative Medicine, the First Affiliated Hospital of Xi'an Jiaotong University, Xi'an 710061, China*

pound materials have attracted extensive research attention.[30] With fast carrier mobility, adjustable direct bandgaps, and small effective mass, III–V compound materials have found significant use in high-speed nanoscale photodetectors, high-frequency electronic devices, and gas sensors.[31–33] As a direct-bandgap III–V compound semiconductor, InSb possesses a small bandgap and high electron mobility, making it a good candidate for optoelectronic materials. The high carrier mobility makes it convenient for the preparation of transistors with high switching speeds. With a large surface-to-volume ratio, the carrier transition time is shortened and the lifetime of photon-generated carriers is extended, leading to a high signal-to-noise ratio for photodetector applications.[34] In addition, the nonlinear optical features of InSb materials were demonstrated.[35,36] Thus, it stimulates research on the generation of ultra-short pulses with enhanced average output power based on InSb SAs. Therefore, it is of high importance to continue to study ultrafast photonic applications of InSb materials.

In this study, an InSb film was grown on the tapered region of a microfiber *via* the magnetron sputtering deposition method. The structure of the electronic band and density of states of InSb were theoretically calculated using the Vienna *ab initio* Simulation Package (VASP) method. The nonlinear saturable absorption features of the InSb-microfiber were measured with a modulation depth of 23.5%, a saturable intensity of 119.8 MW cm^{-2}, and a non-saturable loss of 27.3%. By incorporating the prepared InSb-microfiber SA into an Er-doped fiber (EDF) ring cavity, a Q-switched fiber laser was readily established. Under a pump power of 190 to 480 mW, the pulse width decreased from 6.179 to 1.756 μs, and the output power enhanced linearly from 6.11 to 20.95 mW. The largest single-pulse energy was 221.95 nJ. By carefully optimising the fiber cavity structure and the pump power level, a mode-locking state was established with an ultrafast laser pulse output. The center wavelength was 1544.77 nm with a pulse duration and repetition frequency of 265 fs and 49.51 MHz, respectively. The second-harmonic mode-locked state was realised as the pump power increased from 650 to 780 mW, and the highest output power was 13.22 mW. Compared with the reported laser performance based on 2D material SAs, the obtained Q-switched and mode-locked results show some improvement. This study not only proves that InSb materials possess significant potential for use in ultrafast photonics, but also inspires new applications of InSb materials in nonlinear optics.

Experimental results

Band structure calculations

InSb semiconductors crystallise in a zinc-blend structure with the space group $F\bar{4}3m$. Fig. 1a and b show the atomic structural diagrams of bulk InSb. The Sb and In atoms occupy the (0.25, 0.25, 0.25) and (0, 0, 0) sites, respectively, and their lattice constant is 6.4794 Å. The electronic band structure of

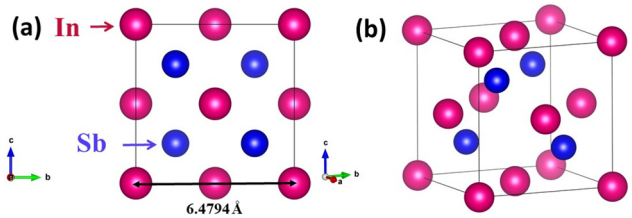

Fig. 1 (a) Top view of bulk InSb and (b) atomic structure of bulk InSb.

bulk InSb, which shows direct bandgap semiconductor characteristics, is illustrated in Fig. 2a. The smallest value of the conduction band and the biggest value of the valence band are situated at the same position between points U and Γ in the first Brillouin area. The bandgap was determined to be 0.187 eV. The eigenvalue of the valence band minimum (VBM) was −0.1 eV, and the eigenvalue of the conduction band minimum (CBM) was 0.087 eV. The effects of different types of atoms on the energy band structures are demonstrated in different colours. Red indicates that Sb atoms have the main effect in the energy band, whereas blue indicates a significant effect induced by Sb atoms. The highest point of the valence band and the lowest point of the conduction band depend on the combined action of the In and Sb atoms. The bandgap is the threshold of the absorbed photon energy, corresponding to electron transitions from the first valence band to the first conduction band. Generally, photon absorption at the bandgap edge is not the most significant. To further study the optical response, the band-nesting properties of InSb were studied. Band-nesting denotes the divergence of the joint density of states (DOS), which indicates a large optical conductivity.[37] When the energy of the top valence band (E_{v1}) and that of the bottom conduction band (E_{c1}) satisfy eqn (1), the band-nesting phenomenon is said to occur:

$$|\nabla(E_{c1} - E_{v1})| \ll 1/(2\pi/a) \quad (1)$$

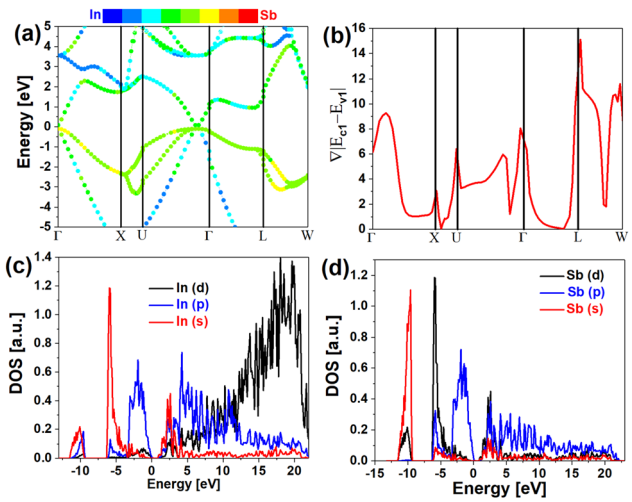

Fig. 2 (a) Band structure of bulk InSb; (b) modulus of a gradient of difference for bulk InSb; (c) DOS of In atoms; and (d) DOS of Sb atoms.

where $2\pi/a$ means the modulus of the reciprocal lattice vector and a is the lattice constant (6.4794 Å). The modulus of the gradient of the difference between E_{c1} and E_{v1} for bulk InSb is shown in Fig. 2b. It is observed that the band-nesting phenomenon appears in two areas. One is between U and X of the high-symmetry k-points, and the other is between Γ and L. Additionally, the relationship between the DOS of In and Sb was also investigated. As shown in Fig. 2c and d, it could be found that the CBM of bulk InSb is dominated by the p states of In and p states of Sb atoms, while the s and p states of In atoms and d and p states of Sb atoms constitute the VBM of bulk InSb.

Materials characteristics

The magnetron sputtering deposition technique is an excellent method for fabricating good SA material films on a large scale with high purity through the growth of 2D materials directly on the substrate, which is beneficial for the formation of high-power ultrafast pulses. Therefore, the magnetron sputtering deposition method was used in this experiment. Additionally, an InSb thin film grown on a Si substrate under the same growth condition was used to study the material characteristics. A scanning electron microscopy (SEM) photograph is presented in Fig. 3a. A compact InSb film was grown on the entire microfiber. To study the physical morphology of the InSb film in more detail, an SEM test of the InSb film on the Si substrate was also performed. As shown in Fig. 3b, the surface morphology of the prepared InSb film indicates that the surface was quite fairly neat and smooth. Fig. 3c shows an atomic force microscopy (AFM) image of the InSb film on the Si substrate, and a line is marked along the cross-section. As demonstrated in Fig. 3d, the thickness of the InSb film was determined to be 4.2 nm. The chemical composition of the obtained InSb film was tested by energy-dispersive X-ray (EDX) spectroscopy. Fig. 3e reveals the EDX spectra, and the signals corresponding to the In and Sb atoms are observed. The atomic ratios of In (1.19%) and Sb (1.48%) are close to 1 : 1. It is noted that the Si signal is very clear. This is because the InSb film on the Si substrate was too thin, resulting in a strong Si signal in the EDX test process. The surface chemical states of the films were characterized by X-ray photoelectron spectroscopy (XPS). Fig. 3f shows the full XPS spectrum of the InSb film, and the measured peaks are marked. The Sb XPS spectrum of InSb is illustrated in Fig. 3g. The peaks at 527.9 eV and 530.7 eV are assigned to the 3d5/2 core level peak of Sb, and the peaks at 537.3 eV and 540 eV correspond to Sb 3d3/2. Fig. 3h shows the XPS spectra of the In signal, and two strong peaks at approximately 452.3 eV and 444.6 eV are assigned to the 3d3/2 and 3d5/2 core level peaks of In, respectively. The measured results are in agreement with those of a previous study.[36]

Nonlinear optical properties of InSb-microfiber SA

The optical response properties of the InSb-microfiber SA for different light intensities were researched using a balanced twin-detector method. A mode-locked EDF laser was utilized as the optical source with a pulse width of 300 fs and a repetition rate of 18.78 MHz. The center wavelength was 1557.8 nm. The measurement setup is illustrated in Fig. 4a. An attenuator was used to regulate the output power of the optical source, and the output laser pulse train was split into two equal parts *via* a 50/50 optical coupler. One beam was directly measured using a power meter, and the other beam was detected after the InSb-microfiber SA. The experimental results obtained along with the nonlinear curve are presented in Fig. 4b. Eqn (2) was used for fitting the experimental data to analyse the nonlinearity of the SA:

$$\alpha(I) = \frac{\alpha_s}{1 + \frac{I}{I_{sat}}} + \alpha_{ns} \quad (2)$$

where $T(I)$, α_s, I_{sat}, and α_{ns} are the transmittance, modulation depth, saturable intensity, and non-saturable loss, respectively. Based on the fitted results, the modulation depth, saturable intensity, and non-saturable loss of the InSb-microfiber SA

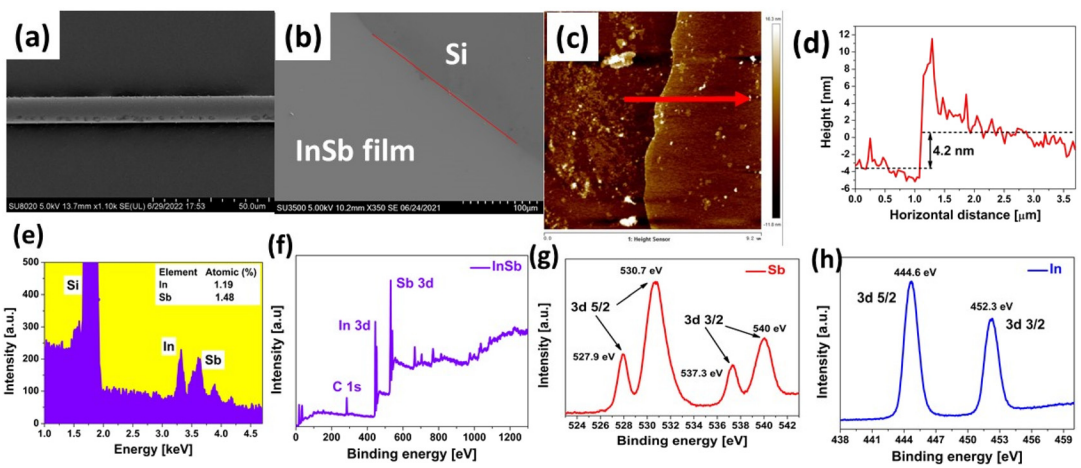

Fig. 3 (a) SEM image of the InSb-microfiber; (b) SEM graph of the InSb film on a Si substrate on 1 mm scale; (c) AFM graph; (d) the height profile; (e) the EDX spectra of InSb; (f) the full XPS spectrum of InSb; (g) the XPS spectrum of the Sb atom; and (h) the XPS spectrum of the In atom.

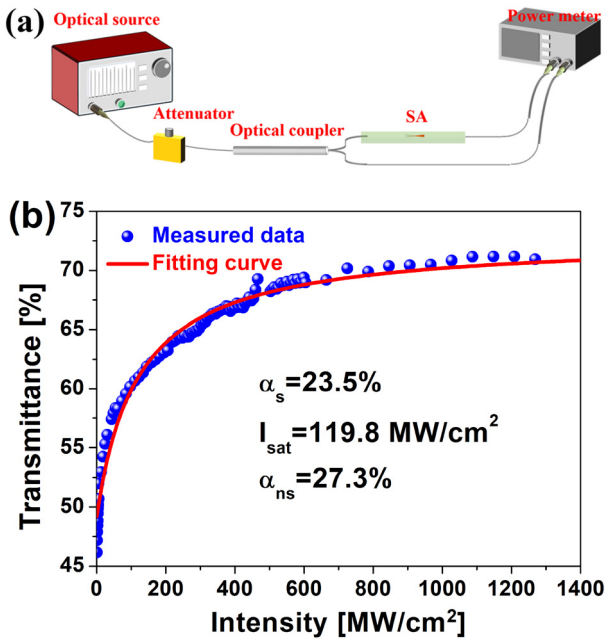

Fig. 4 (a) The balanced twin-detector measurement and (b) the nonlinear optical transmittance properties of the InSb-microfiber SA.

were estimated to be 23.5%, 119.8 MW cm^{-2}, and 27.3%, respectively.

Q-switched fiber laser performance

The setup of the EDF laser cavity with the InSb-microfiber SA is displayed in Fig. 5. A 976 nm laser diode (LD) with a largest power of 650 mW acted as the pump source. A composite optical device with three ports, called a polarisation-independent-isolator-wavelength-division-multiplexer (WDM-ISO), guided the pump light into the fiber cavity, whose pigtail fiber (SMF-28e) is 94.5 cm. Another function is to ensure single-direction light propagation. The gain medium was a segment of EDF (Er 110-4/125) 36.5 cm in length. Through a 50/50 output coupler (OC) with a pigtail fiber (HI 1060) of 2 m, the laser pulses were coupled out from this fiber cavity. The InSb-microfiber SA was inserted into the cavity to generate laser pulses with a length of 73 cm. A polarisation controller (PC) was used to regulate the polarisation conditions of the light in this cavity. The entire cavity length was calculated to be 4.04 m. The dispersion parameters of the EDF, HI 1060, and SMF-28e were approximately 12, −1.3, and −22 fs^2 mm^{-1}, respectively. The net dispersion was calculated to be −0.035 ps^2.

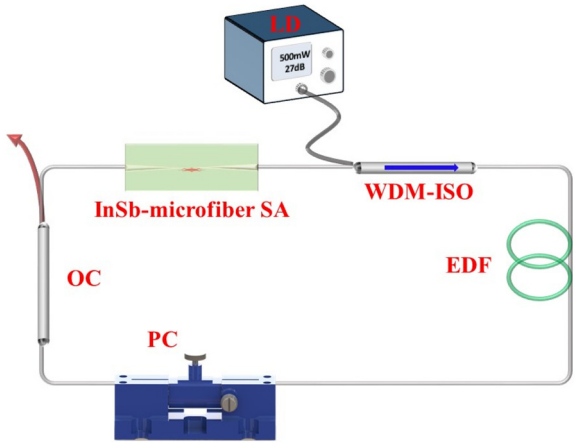

Fig. 5 The setup of the Q-switched EDF laser.

When the pump power reached 190 mW and the PC was optimally regulated, a Q-switched pulse sequence was detected. The pump power for the Q-switched working state was maintained at 480 mW. The variation in these Q-switched pulse sequences with the increment of pump power is presented in Fig. 6a. In the whole process of regulating the pump power, the pulse trains were always in a stable state, and no obvious intensity modulation was observed. It should be noted that the pulse repetition frequency gradually enhanced as the pump power enhanced. At pump powers of 190, 300, 400, and 480 mW, the pulse repetition rates were 44.515, 66.091, 82.788, and 92.96 kHz, respectively. The optical spectrum is depicted in Fig. 6b, from which we can observe that the center wavelength is 1531 nm, which remained unchanged as the pump power was adjusted to 480 mW. A single-pulse profile was recorded at a fixed pump power of 480 mW. As displayed in Fig. 6c, no top amplitude fluctuations existed, and the pulse duration was determined to be 1.756 μs. To study the stability of this Q-switched state, we also tested the radio frequency (RF) spectrum, as displayed in Fig. 6d. The RF peak was located at 92.22 kHz, and its signal-to-noise ratio (SNR) was 60

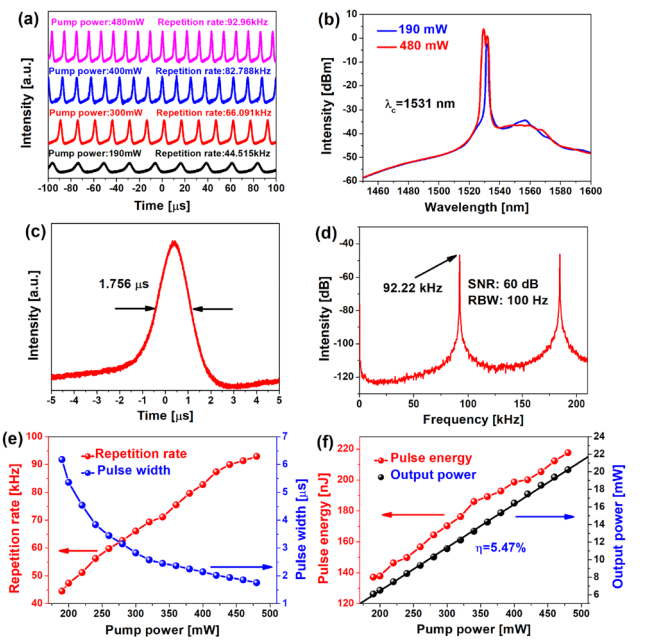

Fig. 6 Q-switched experimental results: (a) digital oscilloscope image; (b) optical spectrum; (c) single-pulse shape; (d) the RF spectrum; (e) the change of pulse duration and repetition rate; and (f) the variation output power and single-pulse energy.

dB. Fig. 6e demonstrates the repetition rate and pulse width as functions of pump power. This shows the representative characteristics of the Q-switched working state. The repetition frequency increased from 44.515 to 92.96 kHz as the pump power enhanced from 190 to 480 mW. The pulse width decreased from 6.179 to 1.756 μs with an increase in pump power. At a low pump power, the pulse duration decreased significantly because electrons accumulated rapidly in the upper energy level. At a high pump power, the speed of accumulation decelerated owing to saturation, which resulted in a slow change in the pulse width. Fig. 6f presents the single-pulse energy and output power variation curves as the pump power is enhanced. The average output power expanded linearly from 6.11 mW to 20.95 mW and the slope efficiency was calculated to be 5.47%. Simultaneously, the single-pulse energy increased with an increment in the pump power, and the highest single-pulse energy was 221.95 nJ.

Mode-locked fiber laser performance

A passive mode-locking operation was not achieved based on the current fiber cavity design. This may be because a balance between dispersion and nonlinearity has not been reached. Therefore, we built another fiber cavity, as displayed in Fig. 7. A 976 nm LD acted as the pump source. The pump light was guided into the fiber cavity *via* a wavelength division multiplexer (WDM) with a 70 cm pigtail fiber (HI 1060). The gain medium was a piece of EDF (Er 110-4/125) with a length of 40 cm. A polarization-independent isolator (ISO) with an HI 1060 fiber length of 100 cm was spliced into the cavity to guarantee single-direction light propagation. The laser was coupled through a 50/50 output coupler (OC) with a 136 cm pigtail fiber (OFS 980). An InSb-microfiber SA with a length of 70 cm was inserted into the cavity. A PC was added to regulate the polarisation of the light in this cavity. The entire cavity length was calculated to be 4.16 m. The dispersion parameter of OFS 980 was approximately 4.5 fs^2 mm^{-1}. The net dispersion was calculated to be −0.0067 ps^2.

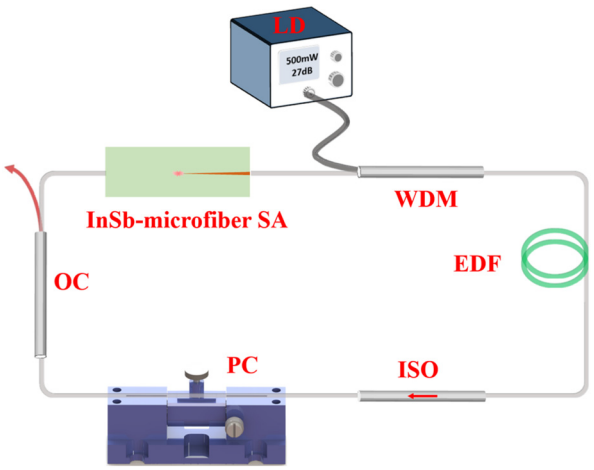

Fig. 7 The setup of a mode-locked EDF laser.

When the fiber cavity was connected, a fundamental mode-locked pulse sequence was obtained as the pump power was increased to 450 mW, and the PC was regulated. The fundamental mode-locked optical spectrum is displayed in Fig. 8a. The center wavelength (λ_c) of this spectrum was 1544.77 nm, and the 3 dB ($\Delta\lambda$) bandwidth was 27 nm. Fig. 8b shows the mode-locked pulse sequence. The time period of this pulse train was 20.185 ns, which matched with the fiber cavity length of 4.16 m exactly, illustrating that the fiber laser operated in the fundamental mode-locking state. Fig. 8c shows the RF spectra of these mode-locked pulses to demonstrate their stability. The fundamental frequency was 49.51 MHz and its SNR reached a maximum of 70 dB. The inset of Fig. 8c provides a harmonic frequency over a span of 550 MHz. The first peak was at 49.51 MHz, and the frequency interval between two neighboring peaks was 49.51 MHz, indicating that the mode-locked laser pulse was in a stable condition. Fig. 8d reveals the measured autocorrelation trace of the pulse with a width of 408 fs. When fitted by the $Sech^2$ equation, the pulse width was determined to be 265 fs.

In general, the formation of laser pulses in a fiber laser means that nonlinearity and dispersion reach a balance. By continually enlarging the pump power to 600 mW and keeping the PC unchanged, the fiber laser can still support this mode-locked state. When the pump power is further enhanced, the nonlinearity becomes stronger, and the equilibrium is broken, which can lead to the splitting of pulses from the fundamental mode-locked state to a high-order harmonic mode-locked state. When the PC was fine-tuned and the pump power reached 650 mW, a second-harmonic mode-locking operation was established. The second-harmonic mode-locked optical spectrum is illustrated in Fig. 9a. The λ_c of this spectrum was 1546.5 nm, and the 3 dB ($\Delta\lambda$) bandwidth was 26.4 nm. Fig. 9b displays the corresponding pulse sequence. The time period was 10.084 ns and the pulse sequence had a uniform intensity. The RF spectra of the second-harmonic mode-locking state

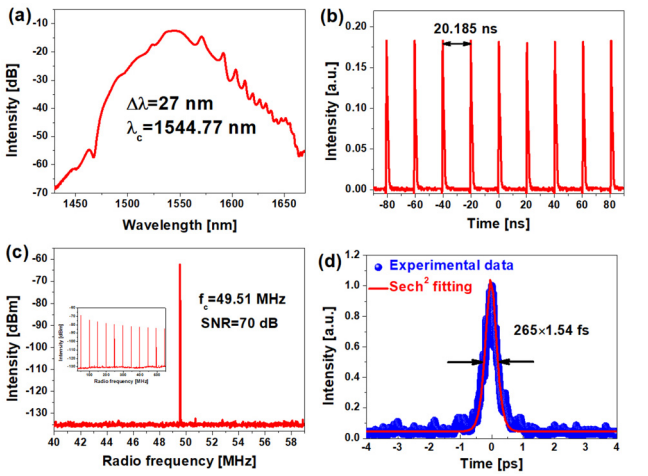

Fig. 8 Fundamental mode-locked experiment results: (a) optical spectra; (b) pulse sequence; (c) RF spectrum; and (d) auto-correlation trace.

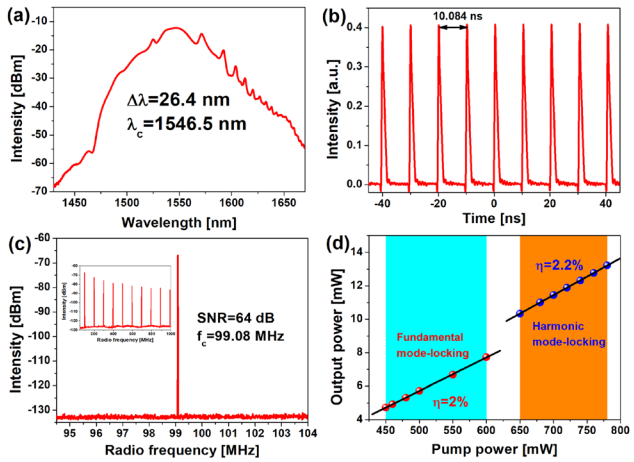

Fig. 9 Second harmonic mode-locked experiment results: (a) optical spectra; (b) pulse sequence; (c) RF spectra; and (d) output power.

were also measured. As presented in Fig. 9c, the signal peak was at 99.08 MHz with an SNR of 64 dB, verifying that the fiber laser operated in the second-harmonic mode-locking state. The RF spectra with a frequency interval of 99.08 MHz over a span of 1 GHz are also given in Fig. 9c, illustrating that the second-harmonic pulse sequence is stable and clear. The second-harmonic mode-locked state could still be supported as the pump power was increased to 780 mW. When the pump power was adjusted to a higher level, the harmonic mode-locked pulses became unstable and disappeared. As exhibited in Fig. 9d, the output power was recorded. The fundamental mode-locked state occurred at a pump power of 450–600 mW, and the output power was enhanced from 4.73 to 7.74 mW. The second-harmonic mode-locking state was maintained as the pump power was enhanced from 650 to 780 mW. The largest output power was 13.22 mW. From the experimental results, it can be determined that the slope efficiency (2%) of the fundamental mode-locked state was less than the slope efficiency (2.2%) of the second-harmonic mode-locked operation.

In this study, there are two modes in the fiber: the transverse magnetic and transverse electric modes, which gain different degrees of interaction with SA materials owing to the different polarisations of each mode, leading to different nonlinear effects of the InSb-microfiber SA. Hence, the polarization condition is a crucial factor in determining the operation mode of the fiber cavity. Thus, the fundamental mode-locked state can be switched to the second-harmonic mode-locked state by changing the polarisation with the PC and regulating the pump power at a high level. When the operational mode is switched, the loss is also altered. Therefore, it can be concluded that the second-harmonic mode-locked state is realised when the InSb-microfiber SA provides a higher transmittance modulation and smaller intra-cavity loss.

The performance of some reported Q-switched and mode-locked EDF lasers with 2D material SAs is summarized in Table 1. The modulation depth of 23.5% obtained herein shows relatively excellent performance among these 2D SA materials, indicating that the InSb-microfiber SA has a strong modulation ability, which is advantageous for ultrafast photonic applications. The Q-switched operation comparison illustrates that the pulse width of 1.756 μs is of the same order of magnitude as that obtained from other 2D SA materials. The output power in this study was as high as 20.95 mW, illustrating an obvious improvement in comparison with the listed results. The SNR value of 60 is comparable to other results, and it also suggests fine stability of the Q-switched operation. It is noted that the pulse width of 265 fs, the average output power of 7.74 mW, and the SNR of 70 dB in mode-locked operation surpass other results obtained from other reports. These results illustrate that the InSb-microfiber SA proposed in this study is an advanced and promising SA candidate for ultrafast photonic applications.

Table 1 Comparison of mode-locked and Q-switched EDF lasers with different 2D material SAs

Operation	SA	ΔT	Output power	Pulse width	SNR	Ref.
Q-switched	MoS_2	2%	5.9 mW	3.3 μs	50	38
	WS_2	4.1%	4.1 mW	2.6 μs	43 dB	39
	$PtTe_2$	0.9%	1.59 mW	2.63 μs	60 dB	40
	$PdSe_2$	2.37%	15.1	2 μs	61 dB	41
	Antimonene	11.63%	4.7 mW	1.4 μs	48 dB	42
	Black phosphorus	18.55%	1.5 mW	10.32 μs	45 dB	43
	In_2Se_3	1.1%	8.1 mW	2.89 μs	57 dB	44
	InSb	23.5%	20.95 mW	1.756 μs	60 dB	This work
Mode-locked	Graphene	7.5%	2.1 mW	345 fs	—	45
	SnS_2	4.6%	1.2 mW	623 fs	45 dB	46
	MoS_2	4.3%	1.78 mW	710 fs	60 dB	47
	Mxene	1.7%	0.05 mW	660 fs	60 dB	48
	Antimonene	6.4%	0.65 mW	552 fs	50 dB	49
	Germanene	9.02%	0.5 mW	901 fs	60 dB	50
	$PdTe_2$	6.83%	0.524 mW	570 fs	60 dB	51
	$GeAs_2$	5.2%	3.5 mW	371 fs	60 dB	52
	InSb	23.5%	7.74 mW	265 fs	70 dB	This work

Conclusions

In conclusion, an InSb film was fabricated on a microfiber by a magnetron sputtering deposition technique, and SEM, AFM, and XPS tests were performed for material characterization. In addition, the structure of the electronic band and density of states of InSb were theoretically studied. The InSb-microfiber SA achieved a saturable intensity of 119.8 MW cm^{-2}, a modulation depth of 23.5%, and a non-saturable loss of 27.3% using the balanced twin-detector technique, respectively. Based on its nonlinear optical saturation properties, the InSb-microfiber SA can realise passively Q-switching and mode-locking operations in two different EDF cavities. In the Q-switched state, a stable Q-switched pulsed laser was obtained with the shortest pulse width of 1.756 μs and largest single-pulse energy of 221.95 nJ. In the mode-locking state, an ultra-short pulse of 265 fs was generated at a wavelength of 1544.77 nm with a repetition frequency of 49.51 MHz. The second-harmonic mode-locked state was acquired, and the highest output power was up to 13.22 mW. These results confirm that InSb is a good SA material, has promising applications for pulsed lasers, and would enhance the research and applications of InSb films in the field of ultrafast optics.

Experimental section

Computational method

The electron–ion interaction was simulated by the projector augmented wave (PAW) scheme in the VASP. In the theoretical calculation process, the exchange correlation is the Green-Wannier version of the Perdew, Burke and Ernzerhof parameterization of the generalized gradient approximation. To improve scattering features at a high energy, pseudopotentials were designed. The cut-off energy was set to 500 eV for energy convergence and static calculations. The Hellmann–Feynman force between every atom was taken as less than 0.01 eV $Å^{-1}$ and the relaxation of energy was set to 1.0×10^{-4} eV. To research the electronic features of the structures as precisely as possible, the HSE06 calculation was performed within the framework of the PAW method. The lattice parameters of the initial structure of the investigated material were obtained from experimentally measured values, and the adopted parameters of the theoretical calculations were tested for convergence.

Microfiber-InSb SA fabrication

First, a microfiber was prepared by stretching a single-mode fiber (SMF-28e) on the machine. The waist diameter was approximately 15 μm, and the length of the taper zone was approximately 1 cm. The microfibers were then fixed at the center of the carrier plate in a vacuum chamber. The angle of the InSb target position was adjusted to make the tapered waist of the microfiber perpendicular to the sputtering direction of the target. Thus, an InSb film was uniformly deposited on the tapered region. The pressure of the chamber was set to 1×10^{-3} Pa using a mechanical pump and a molecular pump. Pure Ar gas was injected into the vacuum chamber. Under the effect of a strong electric field, Ar gas was ionised and it bombarded the InSb target. In this deposition process, the carrier plate was rotated at a constant speed to obtain a uniform InSb film on the microfiber. After the deposition procedure was completed, the RF power was turned off and the chamber pressure was adjusted to atmospheric pressure. Finally, the microfiber coated with the InSb film was removed.

Author contributions

L. H. P. – conceptualization, formal analysis, funding acquisition, investigation, methodology, writing – original draft, and writing – review & editing. R. F. W. – data curation and investigation. Q. Y. Zhao – formal analysis, funding acquisition, and investigation. M. Z. and L. J. – investigation and methodology. X. G. Z. – formal analysis and funding acquisition. R. Q. W. and Y. L. – funding acquisition, project administration, and supervision. W. J. L. – conceptualization, formal analysis, funding acquisition, methodology, and writing – review & editing. All authors have read and approved the manuscript.

Conflicts of interest

There are no conflicts to declare.

Acknowledgements

We acknowledge the financial support from the National Key R&D Program of China (No. 2022YFB4601101); the National Natural Science Foundation of China (NSFC) (No. 11875044 and 62004162); the Key Industry Innovation Chain Project of Shaanxi Province (No. 2022ZDLSF04-09 and 2020ZDLSF04-08); and the New Star Project of Science and Technology of Shaanxi Province (No. 2023KJXX-061).

References

1 K. C. Phillips, H. H. Gandhi, E. Mazur and S. K. Sundaram, Ultrafast laser processing of materials: a review, *Adv. Opt. Photonics*, 2015, **7**(4), 684–712.
2 H. Daido, M. Nishiuchi and A. S. Pirozhkov, Review of laser-driven ion sources and their applications, *Rep. Prog. Phys.*, 2012, **75**(5), 056401.
3 X. Zhao, H. Jin, J. Liu, J. Chao, T. Liu, H. Zhang, G. Wang, W. Lyu, S. Wageh, O. A. Al-Hartomy, A. G. Al-Sehemi, B. Fu and H. Zhang, Integration and applications of nanomaterials for ultrafast photonics, *Laser Photonics Rev.*, 2022, **16**, 2200386.
4 S. T. M. Akkanen, H. A. Fernandez and Z. P. Sun, Optical Modification of 2D Materials: Methods and Applications, *Adv. Mater.*, 2022, **34**(19), 2110152.

5 S. Zhang, Y. Li, X. Zhang, N. Dong, K. Wang, D. Hanlon, J. N. Coleman, L. Zhang and J. Wang, Slow and fast absorption saturation of black phosphorus: experiment and modelling, *Nanoscale*, 2016, **8**, 17374–17382.

6 X. W. Xing, Y. X. Liu, J. F. Han, W. J. Liu and Z. Y. Wei, Preparation of High Damage Threshold Device Based on Bi_2Se_3 Film and Its Application in Fiber Lasers, *ACS Photonics*, 2023, DOI: **10.1021/acsphotonics.2c01375**.

7 S. Liu, J. Wang, J. Shao, D. Ouyang, W. Zhang, S. Liu, Y. Li and T. Zhai, Nanopatterning Technologies of 2D Materials for Integrated Electronic and Optoelectronic Devices, *Adv. Mater.*, 2022, **34**(52), 2270364.

8 Y. Dai, Q. Yu, X. X. Yang, K. Guo, Y. Zhang, Y. S. Zhang, J. R. Zhang, J. Li, J. Chen, H. Q. Deng, T. H. Xian, X. Wang, J. Wu and K. Zhang, Controllable Synthesis of Narrow-Gap van der Waals Semiconductor Nb_2GeTe_4 with Asymmetric Architecture for Ultrafast Photonics, *ACS Nano*, 2022, **16**(3), 4239–4250.

9 Q. Yu, S. Wang, Y. Zhang, Z. Dong, H. Deng, K. Guo, T. Wang, X. Shi, F. Liu, T. Xian, S. Zhu, J. Wu, Z. Zhang, K. Zhang and L. Zhan, Femtosecond ultrafast pulse generation with high-quality 2H-TaS_2 nanosheets via top-down empirical approach, *Nanoscale*, 2021, **13**, 20471–20480.

10 F. N. Xia, H. Wang, D. Xiao, M. Dubey and A. Ramasubramaniam, Two-dimensional material nanophotonics, *Nat. Photonics*, 2014, **8**(12), 899–907.

11 Z. X. Zhao, Z. M. Zhang, J. T. Li, Z. Y. Shang, G. Q. Wang, J. D. Yin, H. Chen, K. Guo and P. G. Yan, MoS_2 hybrid integrated micro-ring resonator phase shifter based on a silicon nitride platform, *Opt. Lett.*, 2022, **47**(4), 949–952.

12 M. Ono, M. Hata, M. Tsunekawa, K. Nozaki, H. Sumikura, H. Chiba and M. Notomi, Ultrafast and energy-efficient all-optical switching with graphene-loaded deep-subwavelength plasmonic waveguides, *Nat. Photonics*, 2020, **14**(1), 37–43.

13 D. H. Ho, Y. Y. Choi, S. B. Jo, J. M. Myoung and J. H. Cho, Sensing with MXenes: Progress and Prospects, *Adv. Mater.*, 2021, **33**(47), 2005846.

14 L. Li, L. H. Pang, R. F. Wang, X. G. Zhang, Z. Q. Hui, D. D. Han, F. Zhao and W. J. Liu, Ternary Transition Metal Dichalcogenides for High Power Vector Dissipative Soliton Ultrafast Fiber Laser, *Laser Photonics Rev.*, 2022, **16**(2), 2100255.

15 E. L. Cai, C. Qi, X. H. Hu, L. Du, L. H. Hao, S. Y. Zhang, F. Lou, M. R. Wang, T. Li and A. F. Wang, Zirconium pentatelluride as saturable absorber for 2 mu m ultrafast solid-state laser, *J. Mater. Chem. C*, 2023, **11**(11), 3812–3817.

16 L. Li, J. Cheng, Q. Zhao, J. Zhang, H. Yang, Y. Zhang, Z. Hui, F. Zhao and W. Liu, Chromium oxide film for Q-switched and mode-locked pulse generation, *Opt. Express*, 2023, **31**(10), 16872–16881.

17 Y. Fang, Y. Ge, C. Wang and H. Zhang, Mid-infrared photonics using 2D materials: status and challenges, *Laser Photonics Rev.*, 2020, **14**(1), 1900098.

18 S. Ahmed, J. P. Qiao, P. K. Cheng, A. M. Saleque, M. N. A. Ivan, T. I. Alam and Y. H. Tsang, Two-Dimensional Gallium Sulfide as a Novel Saturable Absorber for Broadband Ultrafast Photonics Applications, *ACS Appl. Mater. Interfaces*, 2022, **13**, 61518–61527.

19 X. Tian, R. Wei, M. Liu, C. Zhu, Z. Luo, F. Wang and J. Qiu, Ultrafast saturable absorption in TiS_2 induced by non-equilibrium electrons and the generation of a femtosecond mode-locked laser, *Nanoscale*, 2018, **10**, 9608–9615.

20 H. N. Zhang, S. Sun, X. X. Shang, B. Guo, X. H. Li, X. H. Chen, S. Z. Jiang, H. Zhang, H. Agren, W. F. Zhang, G. M. Wang, C. Lu and S. G. Fu, Ultrafast photonics applications of emerging 2D-Xenes beyond graphene, *Nanophotonics*, 2022, **11**(7), 1261.

21 B. Fu, J. Sun, C. Wang, C. Shang, L. Xu, J. Li and H. Zhang, MXenes: Synthesis, Optical Properties, and Applications in Ultrafast Photonics, *Small*, 2021, **17**(11), 2006054.

22 Y. Xu, X. Shi, Y. Zhang, H. T. Zhang, Q. L. Zhang, Z. Huang, X. Xu, J. Guo, H. Zhang, L. Sun, Z. Zeng, A. Pan and K. Zhang, *Nat. Commun.*, 2020, **11**(1), 1–8.

23 C. Gong, Y. Zhang, W. Chen, J. Chu, T. Lei, J. Pu, L. Dai, C. Wu, Y. Cheng, T. Zhai, L. Li and J. Xiong, Electronic and optoelectronic applications based on 2D novel anisotropic transition metal dichalcogenides, *Adv. Sci.*, 2017, **4**(12), 1700231.

24 W. Fan, Y. Han, S. Chen, S. Sun, X. Zhao, C. Bai, G. Wang, C. Lu, W. Zhang, S. Fu and H. Zhang, Nanosized indium selenide saturable absorber for multiple solitons operation in Er^{3+}-doped fiber laser, *Opt. Express*, 2023, **31**(6), 10176–10190.

25 A. Martinez and S. Yamashita, 10 GHz fundamental mode fiber laser using a graphene saturable absorber, *Appl. Phys. Lett.*, 2012, **101**(4), 041118.

26 W. J. Liu, L. H. Pang, H. N. Han, M. L. Liu, M. Lei, S. B. Fang, H. Teng and Z. Y. Wei, Tungsten disulfide saturable absorbers for 67 fs mode-locked erbium-doped fiber lasers, *Opt. Express*, 2017, **25**(3), 2950–2959.

27 X. Jin, G. Hu, M. Zhang, Y. Hu, T. Albrow-Owen, R. C. Howe, T. C. Wu, Q. Wu, Z. Zheng and T. Hasan, 102 fs pulse generation from a long-term stable, inkjet-printed black phosphorus-mode-locked fiber laser, *Opt. Express*, 2018, **26**(10), 12506–12513.

28 W. J. Liu, M. L. Liu, X. M. Liu, M. Lei and Z. Y. Wei, SnSSe as a saturable absorber for an ultrafast laser with superior stability, *Opt. Lett.*, 2020, **45**(2), 419–422.

29 H. L. Chen, L. F. Gao, Z. P. Qin, Y. Q. Ge, K. Khan, Y. F. Song, G. Q. Xie, S. X. Xu and H. Zhang, Recent advances of low-dimensional materials in Mid- and Far-infrared photonics, *Appl. Mater. Today*, 2020, **21**, 100800.

30 N. Han, F. Wang, J. J. Hou, S. P. Yip, H. Lin, F. Xiu, M. Fang, Z. Yang, X. Shi, G. Dong, T. F. Hung and J. C. Ho, Tunable Electronic Transport Properties of Metal-Cluster-Decorated III-V Nanowire Transistors, *Adv. Mater.*, 2013, **25**(32), 4445–4451.

31 Z. Liu, T. Luo, B. Liang, G. Chen, G. Yu, X. Xie, D. Chen and G. Shen, High-detectivity InAs nanowire photodetectors with spectral response from ultraviolet to near-infrared, *Nano Res.*, 2013, **6**(11), 775–783.

32 R. K. Paul, S. Badhulika and A. Mulchandani, Room temperature detection of NO_2 using InSb nanowire, *Appl. Phys. Lett.*, 2011, **99**(3), 033103.
33 T. Takahashi, K. Takei, E. Adabi, Z. Fan, A. M. Niknejad and A. Javey, Parallel array InAs nanowire transistors for mechanically bendable, ultrahigh frequency electronics, *ACS Nano*, 2010, **4**(10), 5855–5860.
34 S. Zhang, H. Jiao, X. Wang, Y. Chen, H. Wang, L. Zhu, W. Jiang, J. Liu, L. Sun, T. Lin, H. Shen, W. Hu, X. Meng, D. Pan, J. Wang, J. Zhao and J. Chu, Highly sensitive InSb nanosheets infrared photodetector passivated by ferroelectric polymer, *Adv. Funct. Mater.*, 2020, **30**(51), 2006156.
35 S. Hou, C. Lu, H. Lin, J. Wang, C. Guo, J. Chen, M. Zhang and P. Yan, Ultrafast thulium-doped fiber laser mode-locked by antimonides, *Opt. Express*, 2021, **29**(9), 13722–13732.
36 Y. Wang, Y. Chen, X. Li, S. Lv, J. Hu, Z. Zhang, X. Wangc and H. Chen, Optical-intensity modulator with InSb nanosheets, *Appl. Mater. Today*, 2022, **21**, 100852.
37 A. Carvalho, R. Ribeiro and A. C. Neto, Band Nesting and the Optical Response of Two-Dimensional Semiconducting Transition Metal Dichalcogenides, *Phys. Rev. B: Condens. Matter Mater. Phys.*, 2013, **88**, 115205.
38 Y. Huang, Z. Luo, Y. Li, M. Zhong, B. Xu, K. Che, H. Xu, Z. Cai, J. Peng and J. Weng, Widely-tunable, passively Q-switched erbium-doped fiber laser with few-layer MoS_2 saturable absorber, *Opt. Express*, 2014, **22**(21), 25258–25266.
39 K. Y. Lau, A. A. Latif, M. H. Abu Bakar, F. D. Muhammad, M. F. Omar and M. A. Mahdi, Mechanically deposited tungsten disulfide saturable absorber for low-threshold Q-switched erbium-doped fiber laser, *Appl. Phys. B*, 2017, **123**(8), 1–12.
40 J. He, H. Lu, L. Tao, Y. Zhao, Z. Zheng and B. Zhou, Nonlinear optical properties of $PtTe_2$ based saturable absorbers for ultrafast photonics, *J. Mater. Chem. C*, 2022, **10**(13), 5124–5133.
41 P. K. Cheng, C. Y. Tang, S. Ahmed, J. Qiao, L. Zeng and Y. H. Tsang, Utilization of group 10 2D TMDs-$PdSe_2$ as a nonlinear optical material for obtaining switchable laser pulse generation modes, *Nanotechnology*, 2021, **32**, 055201.
42 J. Yuan, G. Liu, Y. Xin, F. Xing, K. Han, W. Zhang, F. Zhang and S. Fu, Passively Q-switched modulation based on antimonene in erbium-doped ffber laser with a long term stability, *Opt. Mater.*, 2021, **118**, 111256.
43 Y. Chen, G. Jiang, S. Chen, Z. Guo, X. Yu, C. Zhao, H. Zhang, Q. Bao, S. Wen, D. Tang and D. Fan, Mechanically exfoliated black phosphorus as a new saturable absorber for both Q-switching and Mode-locking laser operation, *Opt. Express*, 2015, **23**(10), 12823–12833.
44 N. A. A. Ramlan, R. Zakaria, N. F. Zulkiffi, N. Kasim, R. A. M. Yusoff and A. A. A. Jafry, Indium Selenide as passive saturable absorber for Q-switching in Erbium-doped fiber lasers, *Opt. Fiber Technol.*, 2022, **72**, 102972.
45 G. Sobon, J. Sotor, I. Pasternak, A. Krajewska, W. Strupinski and K. Abramski, Multilayer graphene-based saturable absorbers with scalable modulation depth for mode-locked Er- and Tm-doped fiber lasers, *Opt. Mater. Express*, 2015, **5**(12), 2884–2894.
46 K. D. Niu, R. Y. Sun, Q. Y. Chen, B. Y. Man and H. N. Zhang, Passively mode-locked Er-doped fiber laser based on SnS_2 nanosheets as a saturable absorber, *Photonics Res.*, 2018, **6**, 72.
47 H. Liu, A. P. Luo, F. Z. Wang, R. Tang, M. Liu, Z. C. Luo, W. C. Xu, C. J. Zhao and H. Zhang, Femtosecond pulse erbium-doped fiber laser by a few-layer MoS_2 saturable absorber, *Opt. Lett.*, 2014, **39**(15), 4591–4594.
48 Y. I. Jhon, J. Koo, B. Anasori, M. Seo, J. H. Lee, Y. Gogotsi and Y. M. Jhon, Metallic MXene saturable absorber for femtosecond mode-locked lasers, *Adv. Mater.*, 2017, **29**(40), 1702496.
49 Y. F. Song, Z. M. Liang, X. T. Jiang, Y. X. Chen, Z. J. Li, L. Lu, Y. Q. Ge, K. Wang, J. L. Zheng, S. B. Lu, J. H. Ji and H. Zhang, Few-layer antimonene decorated microfiber: ultra-short pulse generation and all-optical thresholding with enhanced long term stability, *2D Mater.*, 2017, **4**, 045010.
50 H. Mu, Y. Liu, S. R. Bongu, X. Bao, L. Li, S. Xiao, J. Zhuang, C. Liu, Y. Huang, Y. Dong, K. Helmerson, J. Wang, G. Liu, Y. Du and Q. Bao, Germanium nanosheets with dirac characteristics as a saturable absorber for ultrafast pulse generation, *Adv. Mater.*, 2021, **33**(32), 2101042.
51 P. K. Cheng, S. Ahmed, J. Qiao, L. W. Wong, C. F. Yuen, A. M. Saleque, M. N. A. S. Ivan, S. U. Hani, M. I. Hossain, J. Zhao, Q. Wen and Y. H. Tsang, Nonlinear optical properties of two-dimensional palladium ditelluride ($PdTe_2$) and its application as aerosol jet printed saturable absorbers for broadband ultrafast photonics, *Appl. Mater. Today*, 2022, **26**, 101296.
52 S. Liu, G. Li, F. Zhu, H. Huang, J. Lu, J. Qu, L. Li and Q. Wen, $GeAs_2$ Saturable Absorber for Ultrafast and Ultranarrow Photonic Applications, *Adv. Funct. Mater.*, 2022, **32**(17), 2112252.